Supporting Information for "Laboratory acousto-mechanical study into moisture-induced changes of elastic properties in intact granite"

Rui Wu[1], Paul Antony Selvadurai[1], Ying Li[1], Yongyang Sun[2], Kerry Leith[1], Simon Loew[1]

[1]Department of Earth Science, ETH Zürich, Zürich, Switzerland.

[2]Department of Exploration Geophysics, Curtin University, Perth, Australia.

1. Uncertainty analysis in density and porosity

Uncertainties in the density and porosity were subject to the original measurement error (dimension, volume, mass, etc.) on the selected specimen. These original measurements were assumed to be performed independently and randomly. We considered the uncertainty propagation and defined the final uncertainties as the quadratic sum of the original uncertainties (Taylor, 1997, Chapter 3).

We measured the grain density (ρ_{gr}) over two prismoid oven-dried specimens (dimension: 25 mm $\times$ 25 mm $\times$ 40 mm). The uncertainty in the grain density originated from the measurement of *1*) specimen volume using a helium pycnometer and *2*) specimen weight. The volume and weight were measured at a standard deviation of 0.012 to 0.024 cm^3, and a precision of 0.001 g. The uncertainty ($\frac{\delta\rho_{gr}}{\rho_{gr}}$) in the grain density is given as:

$$\frac{\delta \rho_{gr}}{\rho_{gr}} = \sqrt{(\frac{\delta V}{V})^2 + (\frac{\delta m}{m})^2}. \tag{S1}$$

This resulted an uncertainty of 0.05 to 0.1 % (0.0014 to 0.0027 g/cm^3) in the grain density.

We estimated the uncertainties in the bulk density (ρ_b) and total porosity (ϕ_t) over oven-dried cylinders (L=100 mm in length, d50 mm in diameter). Specimen dimensions were independently measured at a precision of 0.01 mm. Their volumes (V) are given as $V = \pi d^2 L/4$. The uncertainty ($\frac{\delta V}{V}$) in volumes is defined as:

$$\frac{\delta V}{V} = \sqrt{(\frac{2\delta d}{d})^2 + (\frac{\delta l}{l})^2}. \tag{S2}$$

This resulted an uncertainty ($\frac{\delta V}{V}$) in volumes of around 0.04 % (or 0.08 cm^3 for cylinder). Bulk density (ρ_b) was calculated using the ratio of weight (m) to volume (V) of the oven-dried cylinder specimen. The weight was measured at a precision of 0.01 g. The uncertainty ($\frac{\delta \rho_b}{\rho_b}$) in the bulk density is given as:

$$\frac{\delta \rho_b}{\rho_b} = \sqrt{(\frac{\delta m}{m})^2 + (\frac{\delta V}{V})^2} \tag{S3}$$

and calculated as around 0.04 % (or 0.001 g/cm^3).

The total porosity (ϕ_t) was derived from the difference between the grain and bulk density as $\phi_t = 1 - \rho_b/\rho_s$. Its uncertainty is given as:

$$\frac{\delta \phi_t}{\phi_t} = \frac{1}{\rho_s - \rho_b}\sqrt{(\frac{\rho_b}{\rho_s}\delta \rho_s)^2 + (\delta \rho_b)^2} \tag{S4}$$

and calculated as 0.2 % over the granite cylinders. This uncertainty is relatively large to the measured ϕ_t (1.9 %).

The water-accessible porosity (ϕ_w) was calculated from the ratio of mass difference between over-dried and vacuum-saturated cylinder specimen and the volume. Its uncertainty is given as:

$$\frac{\delta\phi_w}{\phi_w} = \sqrt{(\frac{\delta m_o}{m_w - m_o})^2 + (\frac{\delta m_w}{m_w - m_o})^2 + (\frac{\delta V}{V})^2} \tag{S5}$$

and calculated as 0.007 % in the total volume of the cylinder specimen. This also suggested that the measurement of ϕ_w is more precise than ϕ_t.

2. Porosimetry through mercury intrusion and nitrogen adsorption

Seven prismoid specimens (20 mm × 6.5 mm × 6.5 mm) were prepared for the mercury porosimetry. Mercury was intruded into the pore spaces up to 400 MPa and its cumulative volume (V_{Hg}) was shown as a function of pressure in the left side in Figure S1 (adapted with permission from Li, Leith, Perras, and Loew (2021)). The cumulative volumes were measured between 2.59 to 6.21 mm^3/g at a precision of 0.01 mm^3/g over seven specimens. The mercury-accessible porosity can be given as $\phi_{Hg} = V_{Hg}\phi_b/1000$ and was shown on the right side in Figure S1. ρ_b was the bulk density with an estimated uncertainty of 0.006 g/cm^3 following Equation S3. Mercury-accessible porosity ranged from to 0.72 % to 1.69 % with an mean porosity of around 1.15 %. The uncertainty in the mercury-accessible porosity is given as:

$$\frac{\delta\phi_{Hg}}{\phi_{Hg}} = \sqrt{(\frac{\delta V_{Hg}}{V_{Hg}})^2 + (\frac{\delta\rho_b}{\rho_b})^2} \tag{S6}$$

and $\delta\phi_{Hg}$ was calculated between 0.003 % to 0.005 % in the total volume of the prismoid specimen for individual measurement. Washburn's equation was adopted to calculate the pore size from the pressure by assuming the cylindrical pore spaces (Washburn, 1921; Njiekak et al., 2018) (see upper axis of Figure S1). Li et al. (2021) suggested that around 70 % of mercury-accessible pore diameters falling below 200 nm. Although Washburn's equation holds for the penetration of mercury through pore throats greater than around 3 nm (Washburn, 1921; Njiekak et al., 2018), intruded mercury volume maintained when the throat diameter was lower around 10 nm. Poorly connected pores and pores with a throat diameter less than 10 nm were not open to mercury even at intrusive pressures up to 400 MPa. These pore volumes were not counted into the mercury-accessible porosity, and could possibly contribute to the difference between the total (1.9 % $\pm$ 0.2 %) and mercury-accessible porosity.

To quantify the pore size distribution below 10 nm, Li, Kerry, Perras, and Simon (2022) conducted the porosimetry of nitrogen adsorption over two specimens (40 mm $\times$ 10.5 mm $\times$ 10.5 mm). In Figure S2, they showed cumulative surface area (red) and pore volume (black) as a function of pore diameter during the nitrogen adsorption over two specimens (symbol cross and circle). They found that around 80 % of the surface area of this granite exhibited pore diameter below 10 nm.

3. P-wave velocity measurement

A suite of characterization tests were performed to measure P wave velocity structure under ambient conditions. We performed 3D ultrasonic tomography (Martiartu & Böhm, 2017) on three cuboidal specimens of granite with a side length of 160 mm under ambient conditions. Three dimensions were along the principle splitting directions and denoted as *G1*, *G2* and *G3*. Travel time information of the first P-wave arrivals from the transmitters to receivers was used. In Figure S3(a), we showed a schematic representation of the ultrasonic tomography setup along the *G1* direction. An array of nine in-house piezoelectric (PZT) transmitter (Selvadurai et al., 2022, model: PCT-MCX) and nine passive PZT receivers (Wu et al., 2021, model: KRNBB-PC) were mounted in two separate aluminum array holders (grey blocks, Fig. S3(a)). PZT transmitters and receivers were in contact with the top and bottom surfaces of the granite cube, respectively. A 300 V impulse source, with a duration of 1 μs, was applied to these PZT transmitters using a pulsing unit (HVP, Elsys Instruments AE-HV-MUX). Each transmitter emitted an impulse source in a sequential manner that was repeated 10 times for each transmitter. Waveforms on the receivers were recorded in the data acquisition system (DAQ) at a sampling rate of 20 MHz and 16 bit resolution (Elsys Instruments TraNET/Lab-AX). This DAQ system was used in the water imbibition experiments.

The specimens were modeled as 6×6×6 cubic elements each having dimensions of 26.7 mm × 26.7 mm × 26.7 mm. We assumed that the waves propagating from transmitter to receiver were approximated by straight rays. The P-wave travel time and distance of each transmitter-receiver pair were stored in two 9×9 arrays, respectively. P-wave velocity structure was derived at the center of each cubic cells using the Moore-Penrose pseudoinverse. For more detail and the mathematical description of the inversion problem the reader is referred to Martiartu and Böhm (2017). To determine the onset of the P-wave arrival at each receiver, we used the Aikake information criterion (AIC) (Akaike, 1974) that has been effective in laboratory ultrasonic studies (Kurz et al., 2005).

In Figure S3(a), there were 81 straight ray paths (dashed grey lines) that sample most of the cells between transmitters and receivers. In Figure S3(b), we showed the P-wave velocity structure along the *G1* direction and no obvious heterogeneity was observed (standard deviation: 68.5 m/s, 1.72 % of the mean value) among cells. Note that the P-wave velocities were omitted in the cells near the outer surfaces (*G2* and *G3*) because of the lack of effective coverage of straight rays.

To check the seismic anisotropy, this procedure was repeated in the *G2* and *G3* directions. P-wave velocity in each orthogonal direction was characterized by 3981 $\pm$ 69, 3977 $\pm$ 60, and 3988 $\pm$ 64 m/s, respectively. The uncertainty was estimated as 1.72 %, 1.53 % and 1.60 %, respectively. Single-peaked normal (or Gaussian) distributions with very close peak values (around 3997, 3995, and 3995 m/s) were shown in the probability density functions of Figure S3(c). To avoid specimen variability, we repeated the tests on other 2 specimens and the overlapping probability histograms of P-wave velocity distribution was presented in Figure S3(d). P-wave velocities were 3914 $\pm$ 74, 3925 $\pm$ 71, and 3982 $\pm$ 64 m/s, respectively. The uncertainty was estimated as as 1.9 %, 1.8 % and 1.6 %, respectively. We can therefore conclude that there was very weak anisotropy, heterogeneity and specimen variability in the elastic wave velocities of Herrnholz granite.

4. Hydrostatic compression test

To further characterize the material, stress dependence tests of the elastic properties of Herrnholz granite were conducted. This was necessary to provide input data for the validation of the elastic modulus dispersion model in saturated nanopore-dominated rocks employed later.

Hydrostatic compression tests were repeated on two Herrnholz granite and one aluminum cylinders (100 mm in length and 50 mm in diameter) that underwent a stepwise increase in confining pressure from 0 to 160 MPa. The Herrnholz granite specimens were tested under both oven-dried and fully saturated conditions. The aluminum specimen was the reference test, using the same loading procedures. Specimens were tightly wrapped in a rubber jacket and placed into a conventional triaxial machine, LabQuake, located in the Rock Physics and Mechanics Laboratory at ETH Zurich. The system can achieve confining pressures up to 170 MPa and exhibits a minimum frame stiffness of 2500 kN/mm. P- and S-wave transmitter-receiver pairs, installed in the two loading platens, were assembled with specimens at two ends to generate P or S waves at a resonant frequency of approximately 1 MHz through the specimen in the axial direction.

During the test, the confining pressure was increased at a loading rate of 5 MPa/min and was maintained at a series of level (5, 15, 25,..., 160 MPa). The elastic stiffening of the rock specimen in response to the increased pressure was probed by P and S waves. A "square" pulse was emitted every 30 seconds with a duration of 1 μs and a maximum voltage of 12 V. During each loading step, the wave velocity showed low levels of "drift". To accommodate for this, we followed Birch (1960), who recommended setting the duration of the maintained pressure at 30 minutes.

5. Uncertainty analysis in wave velocity

Wave velocity (V) was calculated using the ratio of the specimen length (L) to the transmitted time (t). We found the possible original errors could be: *1*) measurement precision (L_{pre}) of specimen length, 0.01 mm; *2*) parallel tolerance (δL_{para}) between the opposite surfaces, $\pm$ 0.025 mm; *3*) specimen deformation (L_{deform}) during the test; *4*) error in picking arrival times (δt, sampling time). The wave velocity uncertainty can be given using the propagation of error as the quadratic sum of the original uncertainties (Taylor, 1997; Njiekak et al., 2013):

$$\frac{\delta V}{V} = \sqrt{(\frac{L_{pre}}{L})^2 + \frac{L_{para}}{L})^2 + (\frac{L_{deform}}{L})^2 + (\frac{\delta t}{t})^2}. \quad \text{(S7)}$$

For wave velocity measured along the cylinder specimen during the hydrostatic compression tests, L_{deform} has a maximum value of around 0.3 mm at a confining pressure of 160 MPa. The sampling time was 20 ns. We calculated the uncertainties as around 0.32 % (or 18 m/s) for P waves and 0.31 % (or 10 m/s) for S waves, respectively.

For wave velocity measured across the prismoid specimen during the freestanding wetting test, maximum $\frac{L_{deform}}{L}$ was around 2.5×10^{-4} near the transmitter-receiver pair, determined from DIC observation in Section 4.2, due to the hygroscopic expansion. The sampling time was 50 ns. The uncertainty in the P-wave velocity was estimated as around 0.25 % (or 13 m/s).

6. Elastic piezosensitivity analysis

Stress dependence of elasticity caused by microcracks in brittle rocks can be described as (Shapiro, 2003):

$$K_{dr}(P_c) = K_{drs}[1 + \theta_s(C_{drs} - C_{gr})P_c - \theta_c\phi_{c0}\exp(-\theta_c P_c C_{drs}), \quad \text{(S8a)}$$

$$G_{dr}(P_c) = G_{drs}[1 + \theta_{sg}(C_{drs} - C_{gr})P_c - \theta_{cg}\phi_{c0}\exp(-\theta_c P_c C_{drs}), \quad \text{(S8b)}$$

where K_{dr}, G_{dr} and P_c were measured in the hydrostatic compression tests. The pore space of the rock (ϕ) was assumed to consist of stiff and compliant/crack pores, which formed a fully interconnected pore space. ϕ_{c0} denoted the compliant porosity without confinement: the porosity of the stiff pores (ϕ_s) approximated the water-accessible porosity (ϕ_w). The bulk (K_{gr}) and shear (G_{gr}) moduli of granite without pore space in terms of constituents and pore space from Hill average were 49.4 and 31.1 GPa, respectively. We provided the mineral moduli and effective elastic moduli of Herrnholz granite in Table S1. K_{drs} and G_{drs} were the bulk and shear moduli of a hypothetical rock in the case of a closed compliant porosity ($\phi_c \approx 0$). C_{gr} and C_{drs} are the the compressibilities, the reciprocal of K_{gr} and K_{drs}, respectively.

From left to right in Equation S8a and S8b, 1, linear term and exponential term represented the individual contribution from mineral grains, stiff pores and compliant cracks to moduli, respectively. θ_c and θ_{cg} were the elastic sensitivity of confining pressure on the exponential term of bulk and shear moduli $O(10^2)$, while θ_s and θ_{sg} with the order of $O(1)$ reflected the sensitivity of linear terms:

$$\theta_s = -\frac{1}{K_{drs}}\frac{\partial K_{dr}}{\partial \phi_s}, \quad \theta_c = -\frac{1}{K_{drs}}\frac{\partial K_{dr}}{\partial \phi_c}, \tag{S9a}$$

$$\theta_{s\mu} = -\frac{1}{\mu_{drs}}\frac{\partial \mu_{dr}}{\partial \phi_s}, \quad \theta_{c\mu} = -\frac{1}{\mu_{drs}}\frac{\partial \mu_{dr}}{\partial \phi_c} \tag{S9b}$$

Inputting the measured K_{dry}, G_{dry} and P_c and given the initial guesses for the unknown parameters K_{drs}, G_{drs}, θ_s, θ_{sg}, θ_c, θ_{cg} and ϕ_{c0}, the residuals of S8a and S8b were obtained, summed and minimized to find optimal parameters: $K_{drs} = 49.7$ GPa, $G_{drs} = 29.7$ GPa, $\theta_s = 6.2 \times 10^{-4}$, $\theta_{sg} = 4.8 \times 10^{-4}$, $\theta_c = 701$, $\theta_{cg} = 505$ and $\phi_{c0} = 7.2 \times 10^{-4}$.

The observation of $\theta_s\phi_s \ll \theta_c\phi_c$ (ratio: 1.9×10^{-5}) suggested that the elastic variations strongly depended on changes in the compliant porosity and only depend weakly on changes in the stiff porosity. By assuming that the cracks were penny-shaped within the framework of effective medium theories, the representative aspect ratio α was estimated at approximately 1.1×10^{-3} (Equation 11 from Shapiro (2003); more detail refer to O'Connell and Budiansky (1974)):

$$\alpha \approx \frac{K_{gr}\left(3K_{gr}+4\mu_{gr}\right)}{\pi\theta_c\mu_{gr}\left(3K_{gr}+\mu_{gr}\right)}. \tag{S10}$$

7. P-wave velocity increase from squirt flow model

In this section, we detailed the calculation procedures of P-wave velocity increase at all frequencies in saturated microcracked porous media using a squirt flow model (Gurevich et al., 2010). We showed a schematic diagram of the pore space configuration in microcracked media in Figure S8. The pore space of the rock is assumed to consist of stiff (or round) and compliant pores, which form a fully interconnected pore space. Disk-shaped gap (soft pore) represents microcrack between two grains and its tip opens into two adjacent round pores (or stiff pores). The gap is assumed to have asperities so that it has a finite stiffness even when the gap is dry. When elastic wave propagates in such configuration, infilled water does not have sufficient time to escape from the gap within the half-period of the wave. This gives a frequency-dependent bulk modulus $K_f^*(\omega)$ of water:

$$K_f^*(\omega) = \left[1 - \frac{2J_1(ka)}{kaJ_0(ka)}\right] K_f, \tag{S11}$$

where ω is angular frequency, a is disk radius, J_0 and J_1 are Bessel equation of zero order and first order, K_f is bulk modulus of water. k is wavenumber and is given as $k^2 = -\frac{12i\omega\eta}{h_0^2K_f}$. h_0 is the disk thickness and disappears together with disk radius a in Equation S11 using the aspect ratio $\alpha = \frac{h_0}{2a}$ that is available (1.1×10^{-3}) from elastic piezosensitivity analysis. η is the dynamic viscosity of water ($9.4{\times}10^{-4} Pa \cdot s$ under 23 $°C$ and 1 standard atmosphere).

In Figure S8(a), microcrack was filled with water while the round pores were dry. We applied Gassmann equation (Gassmann, 1951) to calculate partially relaxed bulk modulus K_{mf} and shear modulus G_{mf} of this modified frame under a confining pressure P:

$$\frac{1}{K_{mf}(P,\omega)} = \frac{1}{K_{drs}} + \frac{1}{\frac{1}{K_{\mathrm{dry}}(P)} - \frac{1}{K_{drs}}} + \frac{1}{\left(\frac{1}{K_f^*(P,\omega)} - \frac{1}{K_{gr}}\right)\phi_c(P)}, \tag{S12a}$$

$$\frac{1}{G_{mf}(P,\omega)} = \frac{1}{G_{\mathrm{dry}}(P)} - \frac{4}{15}\left[\frac{1}{K_{\mathrm{dry}}(P)} - \frac{1}{K_{mf}(P,\omega)}\right], \tag{S12b}$$

where K_{drs} and K_{gr} were the bulk modulus of hypothetical granite in the case of a closed compliant porosity ($\phi_c \approx 0$) and without pore space, respectively. $K_{dry}(P)$ and $G_{dry}(P)$ were the bulk and shear modulus of dry rocks at different confining pressure, respectively. $K_{dry}(P)$ and $G_{dry}(P)$ were measured from hydrostatic compression tests (Figure 3(c) and (d)). $\phi_c(P)$ was the compliant porosity at different confining pressure and was available from elastic piezosensitivity analysis (blue dashed line in Figure 3(c)).

In Figure S8(b), both microcrack and round pores were filled with water and we applied the Gassmann equation (Gassmann, 1951) again to calculate bulk modulus K_{sat} and shear modulus G_{sat} of this fully saturated granite under a confining pressure P:

$$\frac{1}{K_{\mathrm{sat}}(P,\omega)} = \frac{1}{K_{gr}} + \frac{\phi_s\left(\frac{1}{K_f} - \frac{1}{K_{gr}}\right)}{1 + \phi_s\left(\frac{1}{K_f} - \frac{1}{K_{gr}}\right) / \left(\frac{1}{K_{mf}(P,\omega)} - \frac{1}{K_{gr}}\right)}, \tag{S13a}$$

$$G_{sat}(P,\omega) = G_{mf}(P,\omega), \tag{S13b}$$

where ϕ_s was porosity of the stiff pores and approximates the water-accessible porosity (ϕ_w). We calculated bulk modulus $K_{sat}(P)$ and shear modulus $G_{sat}(P)$ from squirt flow model at interested frequency bandwidth – 1 MHz in our study. Theoretical prediction of

P-wave velocity $V_p(P)$ under different confining pressure in saturated microcracked media is given as:

$$V_p(P) = \sqrt{\frac{K_{sat}(P) + \frac{4}{3}G_{sat}(P)}{\rho_{sat}}}, \tag{S14}$$

where ρ_{sat} was the density (2.63 g/cm^3) of saturated rock and was assumed not to change with confining pressure.

References

Akaike, H. (1974). A new look at the statistical model identification. *IEEE Transactions on Automatic Control*, *19*(6), 716–723. doi: 10.1109/TAC.1974.1100705

Birch, F. (1960). The velocity of compressional waves in rocks to 10 kilobars: 1. *Journal of Geophysical Research (1896-1977)*, *65*(4), 1083–1102. doi: https://doi.org/10.1029/JZ065i004p01083

Gassmann, F. (1951). Elastic waves through a packing of spheres. *GEOPHYSICS*, *16*(4), 673–685. doi: 10.1190/1.1437718

Gurevich, B., Makarynska, D., de Paula, O. B., & Pervukhina, M. (2010). A simple model for squirt-flow dispersion and attenuation in fluid-saturated granular rocks. *GEOPHYSICS*, *75*(6), N109-N120. doi: 10.1190/1.3509782

Kurz, J. H., Grosse, C. U., & Reinhardt, H. W. (2005, 6). Strategies for reliable automatic onset time picking of acoustic emissions and of ultrasound signals in concrete. *Ultrasonics*, *43*(7), 538–546. doi: 10.1016/J.ULTRAS.2004.12.005

Li, Y., Kerry, L., Perras, M. A., & Simon, L. (2022). Effect of Ambient Humidity on the Elasticity and Deformation of Unweathered Granite. *Journal of Geophysical Research: Solid Earth*.

Li, Y., Leith, K., Perras, M. A., & Loew, S. (2021). Digital image correlation–based analysis of hygroscopic expansion in Herrnholz granite. *International Journal of Rock Mechanics and Mining Sciences*, *146*, 104859. doi: 10.1016/J.IJRMMS.2021.104859

Martiartu, N. K., & Böhm, C. (2017). *TTomo: Straight ray tomography.* Seismology and Wave Physics group at ETH Zurich. Retrieved from `https://cos.ethz.ch/software/research/ttomo.html`

Mavko, G., Mukerji, T., & Dvorkin, J. (2020). *The Rock Physics Handbook*. Cambridge, United Kingdom: Cambridge University Press. doi: 10.1017/9781108333016

Njiekak, G., Schmitt, D. R., & Kofman, R. S. (2018, 12). Pore systems in carbonate formations, Weyburn field, Saskatchewan, Canada: Micro-tomography, helium porosimetry and mercury intrusion porosimetry characterization. *Journal of Petroleum Science and Engineering*, *171*, 1496–1513. doi: 10.1016/J.PETROL.2018.08.029

Njiekak, G., Schmitt, D. R., Yam, H., & Kofman, R. S. (2013, 6). CO2 rock physics as part of the Weyburn-Midale geological storage project. *International Journal of Greenhouse Gas Control*, *16*, S118-S133. doi: 10.1016/j.ijggc.2013.02.007

O'Connell, R. J., & Budiansky, B. (1974). Seismic velocities in dry and saturated cracked solids. *Journal of Geophysical Research (1896-1977)*, *79*(35), 5412–5426. doi: https://doi.org/10.1029/JB079i035p05412

Selvadurai, P. A., Wu, R., Bianchi, P., Niu, Z., Michail, S., Madonna, C., & Wiemer, S. (2022). A Methodology for Reconstructing Source Properties of a Conical Piezoelectric Actuator Using Array-Based Methods. *Journal of Nondestructive Evaluation*, *41*(1), 23. doi: 10.1007/s10921-022-00853-6

Shapiro, S. A. (2003). Elastic piezosensitivity of porous and fractured rocks. *GEOPHYSICS*, *68*(2), 482–486. doi: 10.1190/1.1567215

Taylor, J. (1997). *Introduction to error analysis, the study of uncertainties in physical measurements.*

Washburn, E. W. (1921, 3). The Dynamics of Capillary Flow. *Phys. Rev.*, *17*(3), 273–283. doi: 10.1103/PhysRev.17.273

Wu, R., Selvadurai, P. A., Chen, C., & Moradian, O. (2021). Revisiting piezoelectric sensor calibration methods using elastodynamic body waves. *Journal of Nondestructive Evaluation*, *40*(3), 68. doi: 10.1007/s10921-021-00799-1

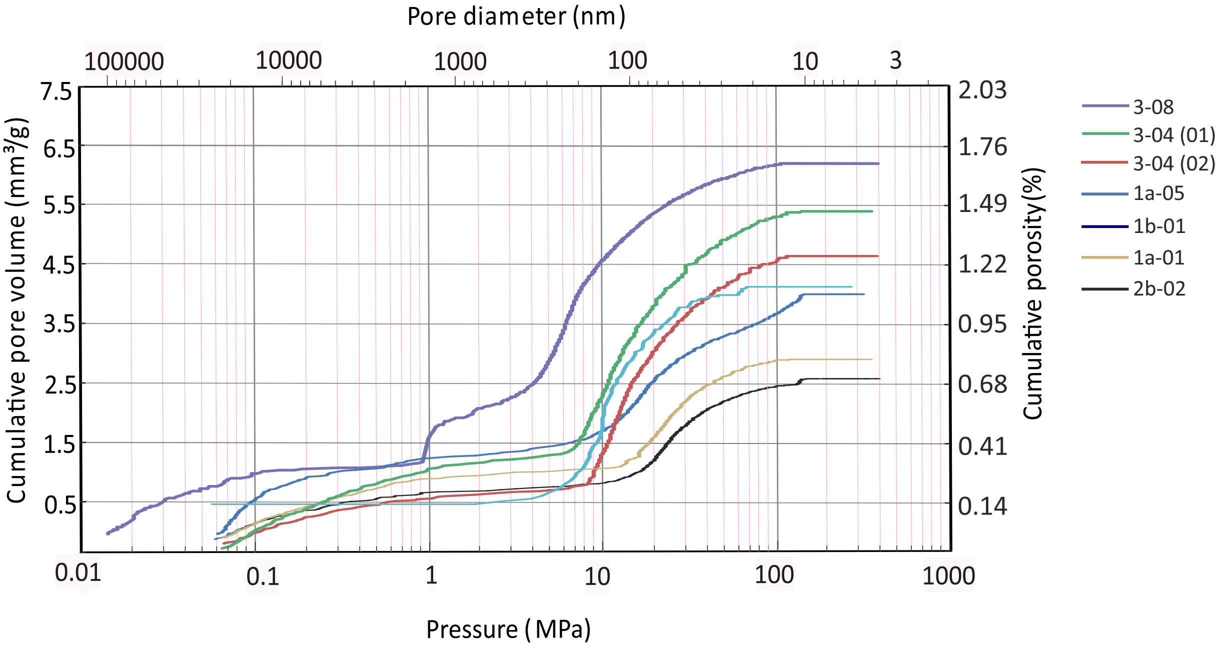

Figure S1. Cumulative volume of intrusive mercury and mercury-accessible porosity as a function of pressure over seven specimens (adapted with permission from Li et al. (2021) (CC BY-NC-ND 4.0)).

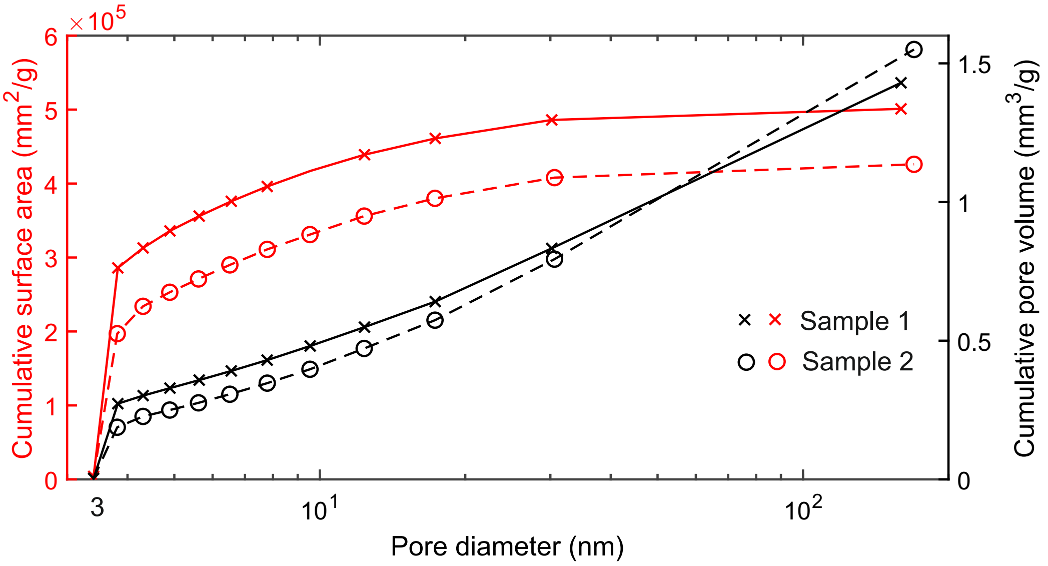

Figure S2. Cumulative pore surface area and volume as a function of pore diameter during nitrogen adsorption over two specimens (adapted with permission from Li et al. (2022)).

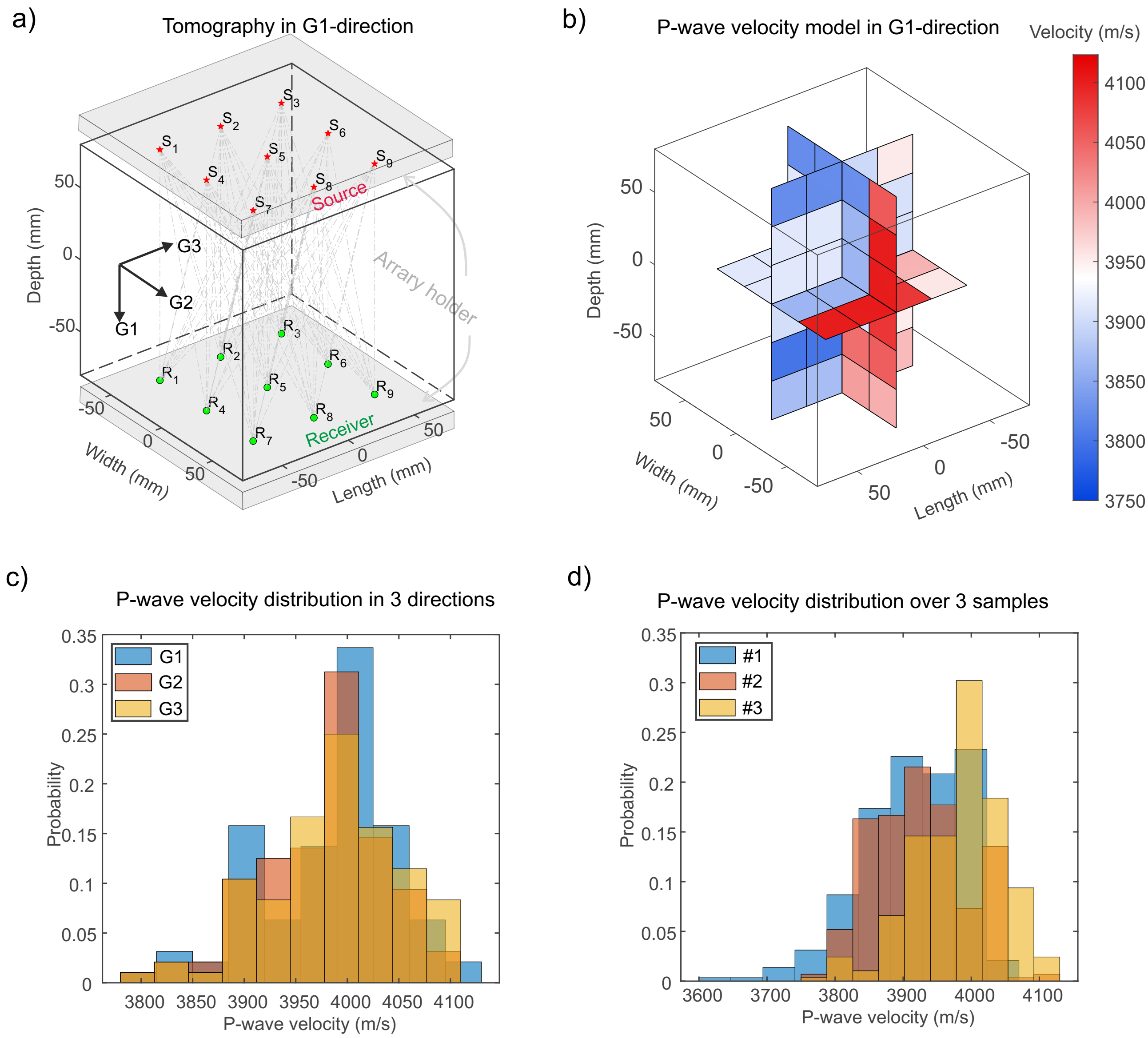

Figure S3. (a) General schematic of the setup to measure P-wave velocity tomography using travel-time tomography. (b) Reconstructed P-wave velocity slices along the *G1* direction. (c) P-wave velocity histograms along the *G1*, *G2* and *G3* directions for 1 specimen. (d) P-wave velocity histograms for the three specimens.

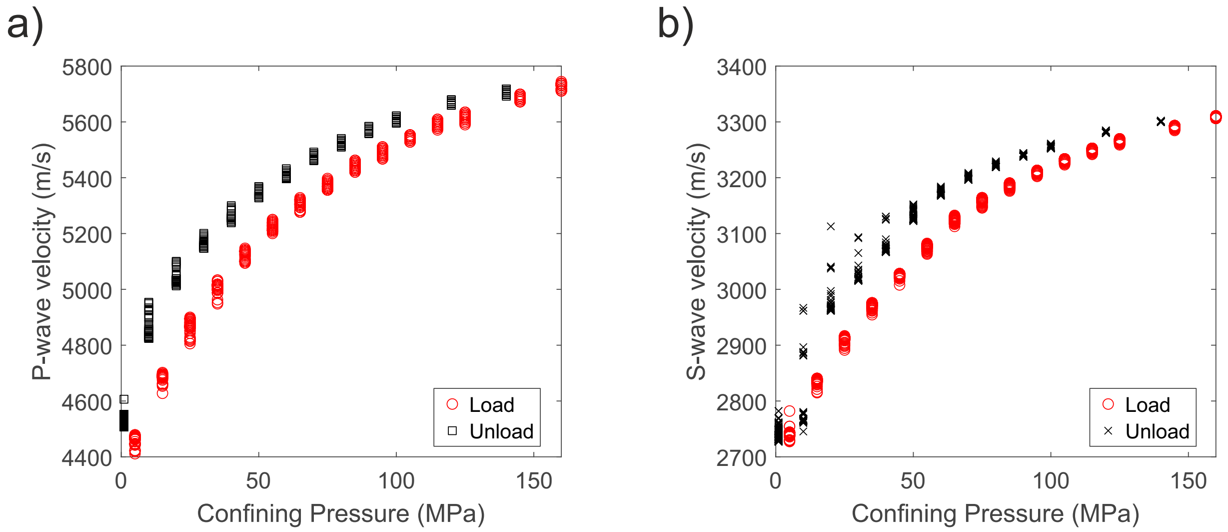

Figure S4. P- (left) and S-wave (right) velocity changes in dry Herrnholz granite in response to a series of confining pressures during the loading (red) and unloading (black) stage.

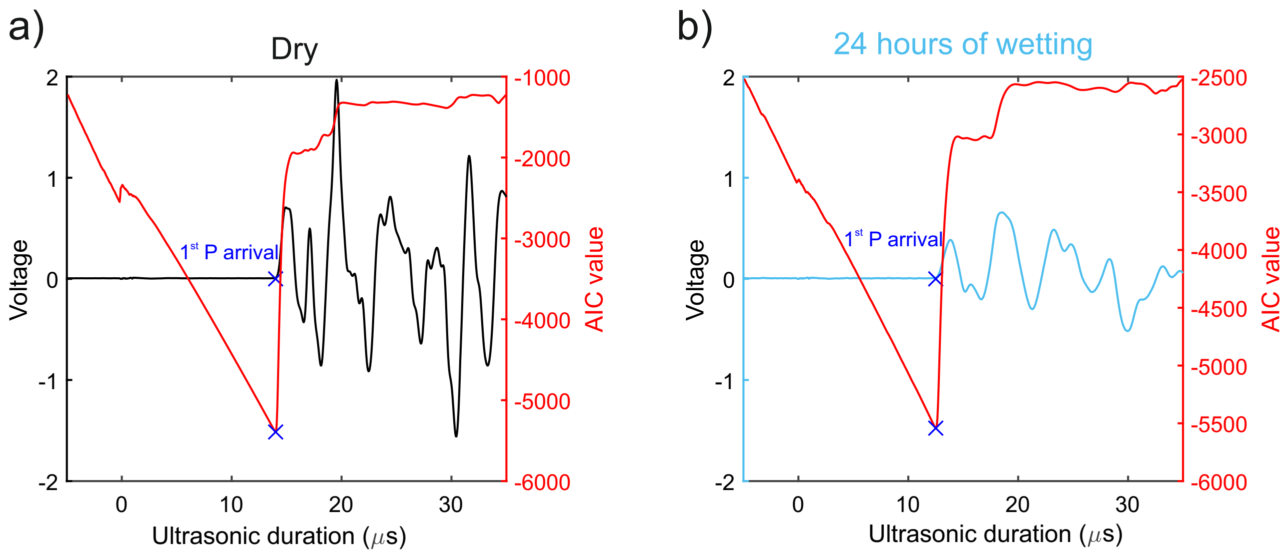

Figure S5. Raw transmitted waveforms and their AIC values under (a) dry and (b) wet conditions. The onset of P-wave first arrival (blue cross) was marked at the position of minimum AIC.

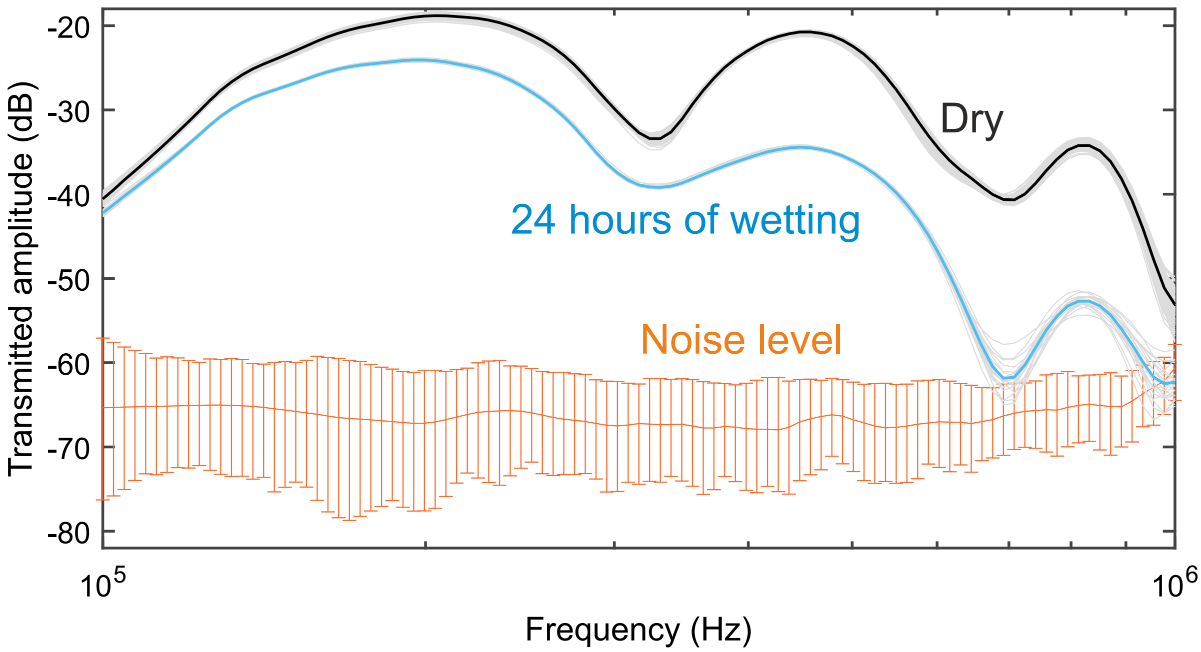

Figure S6. Transmitted amplitude (dB) of windowed waveforms in the frequency domain shown in Figure 4(d) measured (a) under dry conditions and (b) after 24 hours of wetting. Noise level is given as the reference. Transmitted amplitude above 1 MHz after 24 hours of wetting is hard to be differentiable from the noise level.

Table S1. Mineral moduli and effective elastic moduli of Herrnholz granite

	Quartz	Feldspar (plagioclase)	Mica (Biotite)	Voigt bound	Reuss bound	Hill average
Fraction (%)	50	38	11			
Bulk modulus (GPa)	37	75.6	41.1	51.7	47.1	49.4
Shear modulus (GPa)	44	25.6	13.4	33.2	29.1	31.1

Moduli of common minerals come from Mavko, Mukerji, and Dvorkin (2020, Table A.4.1).

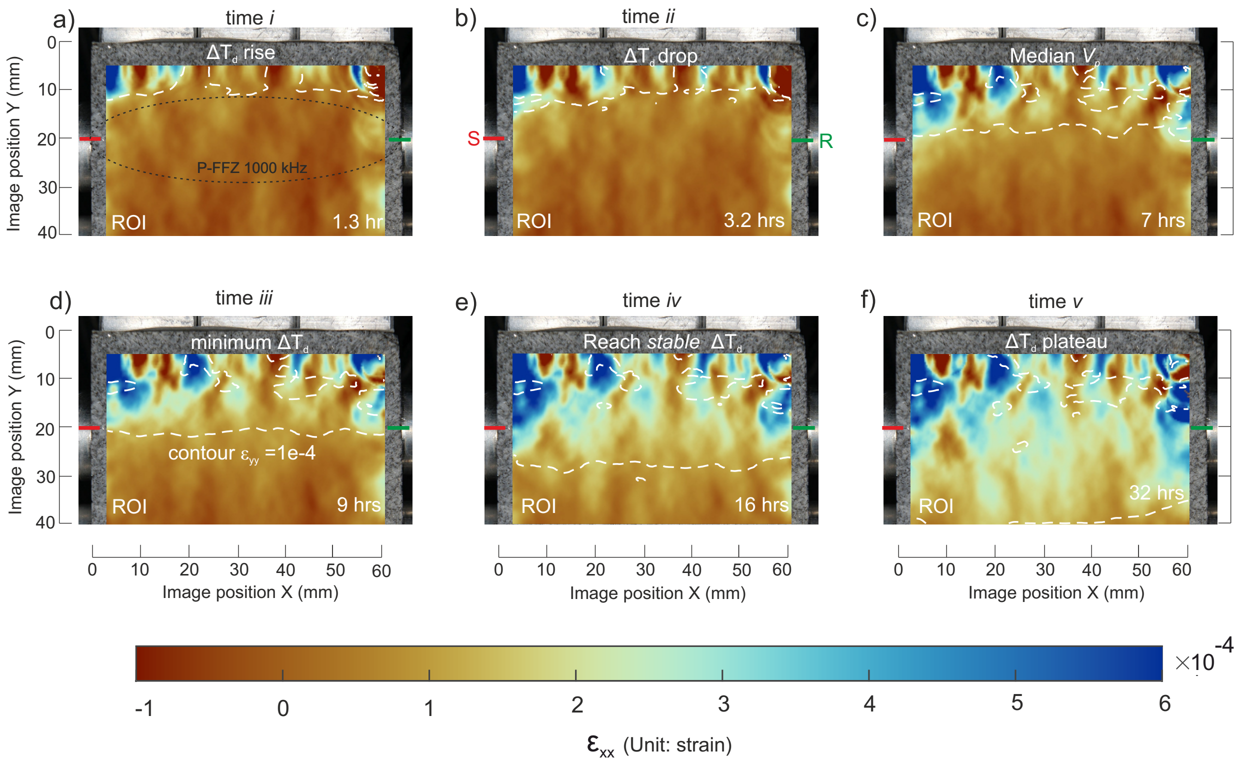

Figure S7. Horizontal strain (ϵ_{xx}) evolution on the front surface (ROI: 58 mm in width and 40 mm in height) with water being applied to the granite specimen. 0 hour denotes the time that water is applied to the top surface of the specimen. Stage *i* to *v* are time moments previously defined in acoustic signature analysis.

Table S2. Summary of ultrasonic attribute changes through the gradual wetting process.

Acoustic changes	**Symbol**	**Unit**	**Freq**	**Stages** O	i	ii	iii	iv	v	**Total**
			LF			↑2.6	↓9	↑0.6		↓ 4.6 ± 1
Transmitted amplitude	ΔT_d	dB	MF	±1	±1	↑3	↓19.5	↑5.5	±0.1	↓ 12.6 ± 1
			HF			↑4	↓27	↑8		↓ 17 ± 1
P-wave velocity	ΔV_p	m/s		±10	↓ 30		↑550		±19	↑ 520 ± 20
Inverse quality factor	$\Delta(1/Q_p)$	1×10^{-3}		±1		↑13		↑37	±5	↑ 50 ± 5

Symbol ± represents the attribute fluctuation due to the background noise levels in the measurements.

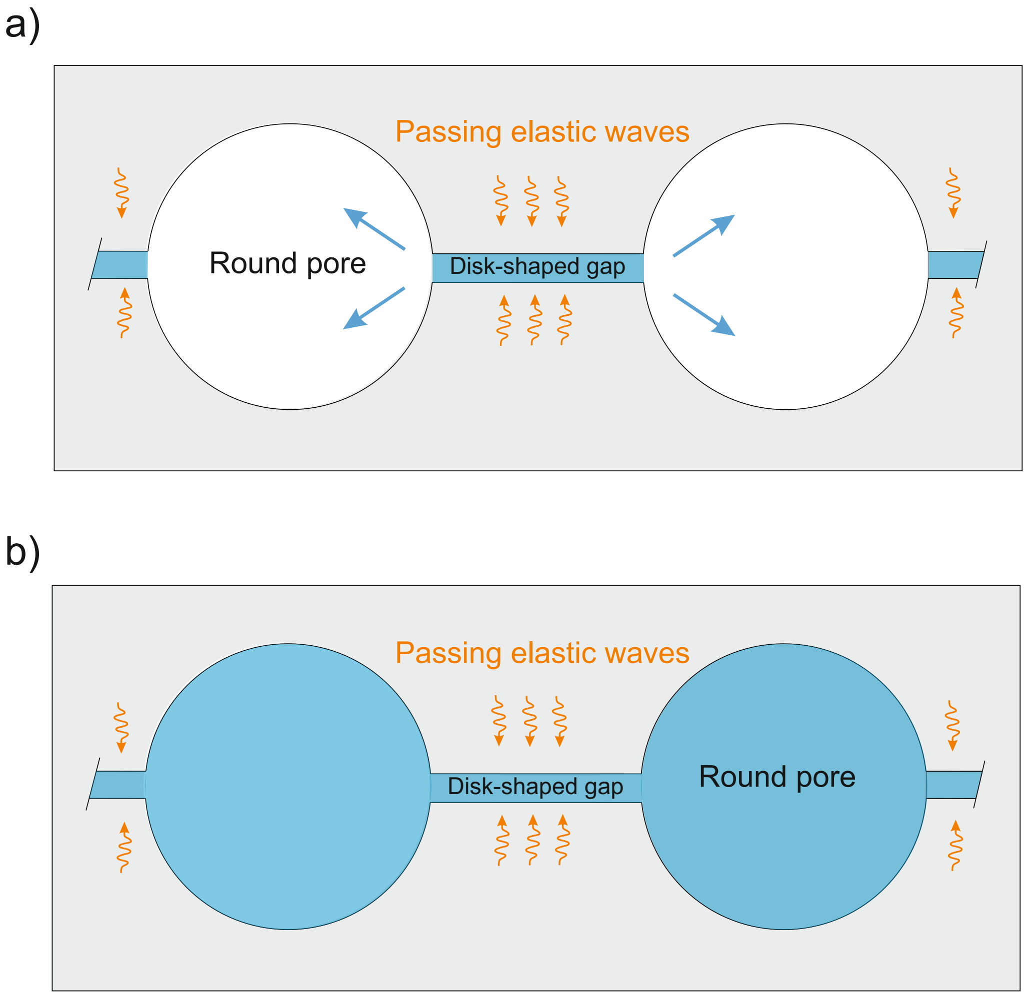

Figure S8. Schematic diagram of the pore space configuration in microcracked media. Disk-shaped gap (soft pore) represents microcrack between two grains and its edge opens into two round pores (or stiff pores). (a) microcrack is filled with water while the round pores are dry. (b) Both microcrack and round pores are filled with water.